Ceramics International xxx (xxxx) xxx

Contents lists available at ScienceDirect

Ceramics International

journal homepage: www.elsevier.com/locate/ceramint

Ultraviolet light charged and self-powered mechanoluminescence of $KMgF_3$: Tb^{3+} glass ceramics in various media

Lili Li, Yingdan Song, Hongxin Song, Kaige Cheng, Qiang Xu **, Lei Zhao *

Baoji Key Laboratory of Micro-Nano Optoelectronics and Terahertz Technology, School of Physics and Opto-Electronic Technology, Collaborative Innovation Center of Rare-Earth Optical Functional Materials and Devices Development, Baoji University of Arts and Sciences, Baoji, Shanxi, 721016, PR China

ARTICLE INFO

Handling Editor: Dr P. Vincenzini

Keywords:
Mechanoluminescence
Glass ceramics
UV charged
Self-powered

ABSTRACT

The light waveguiding effect of transparent glass ceramics (GCs) on mechanoluminescence (ML) signals is highly attractive for remote stress sensing and structural health monitoring applications. However, a prerequisite for generating ML in GCs is pre-irradiation with high-energy rays, which not only increases application costs but also poses a risk of GCs devitrification. Herein, we propose a safe, non-destructive, and convenient charging method for the ML of $KMgF_3$: Tb^{3+} GCs, namely ultraviolet (UV) light charging. By effectively filling the intrinsic defects in $KMgF_3$: Tb^{3+} nanocrystal using UV light, we achieved trap-controlled ML in rigid GCs. Moreover, this ML is attributed to thermoluminescence (TL) induced by frictional heating during mechanical stimulation. Additionally, when the GCs powder is combined with flexible polydimethylsiloxane (PDMS), a self-powered (without any pre-charging) ML induced by interfacial triboelectricity can also be achieved, which is similar to the results observed in most flexible ML systems. This work proposes a more straightforward and safer approach for applications such as mechanical sensing based on the ML of transparent GCs.

1. Introduction

Mechanoluminescence (ML) is a mechanical energy-optical energy conversion process that occurs during mechanical stimuli such as compression, tensile, friction, scraping, and impact, forming a link between luminescence and mechanics, and is widely used in visualization, non-contact mechanical sensing, structural health monitoring, and wearable devices [1–6]. Currently, research on ML materials mainly focuses on inorganic phosphor doped with rare-earth ions or transition metal ions, such as ZnS: Cu+/Mn^{2+} [7], CaZnSO: RE^{3+}/Mn^{2+} [8], $Tb_3Al_5O_{12}$: Ce^{3+} [9], $SrGa_{12}O_{19}$: Cr^{3+} etc [10]. When integrated with organic flexible media (such as PDMS and Epoxy resin (ER)), these materials are capable of generating pronounced ML [11–13]. Based on the mechanism of ML generation, interface triboelectric-type ML does not require additional pre-charging and is a self-powered form of ML [14,15]. However, for rigid glass-ceramics (GCs), the absence of an inorganic-organic interface prevents the generation of self-powered interface triboelectric-type ML. Instead, these materials often require pre-irradiation with high-energy light for charging.

In our research group's previous work, it was found that GCs, due to their unique optical waveguide effect, can enable remote sensing and detection of stress states [16,17]. This is an intriguing phenomenon not observed in inorganic-organic composite ML materials. As mentioned above trap-controlled ML in GCs requires pre-charging with high-energy radiation. During the charging process, the irradiation from high-energy rays can induce some non-intrinsic point defects in the GCs's network structure due to photoionization [18,19], During high-energy irradiation, the process can break bridging oxygen bonds, leading to the formation of non-intrinsic defects such as oxygen vacancies. Additionally, it can induce the creation of color centers within the glass, resulting in reduced transparency. Furthermore, the high-energy radiation required for pre-charging, such as X-ray and femtosecond lasers, is typically harmful and unsafe for humans. In practical applications, the continuous pre-irradiation process not only increases the risk of injury to operators but also adds to the complexity of the procedure. Additionally, the high cost and limited availability of high-energy radiation sources make the pre-charging method particularly cumbersome [20].

By engineering appropriate intrinsic defects within the nanocrystals of the crystalline phase in GCs, and utilizing simple and safe ultraviolet (UV) or visible light for pre-charging, this approach offers a promising

* Corresponding author.
** Corresponding author.
E-mail addresses: xuqiang@bjwlxy.edu.cn (Q. Xu), zhaoleibjwl@163.com (L. Zhao).

https://doi.org/10.1016/j.ceramint.2024.11.044
Received 6 October 2024; Received in revised form 1 November 2024; Accepted 3 November 2024
Available online 4 November 2024

solution to the problem. Cao et al. Reported the near infrared ML in $ZnGa_2O_4$: Cr^{3+} GCs by UV pre-charged [21]. This simple and safe UV pre-charging method for achieving ML not only preserves the high transparency of the glass during the pre-irradiation process but also effectively fills the trap centers caused by intrinsic defects in the material. As a result, the search for ML GCs capable of non-destructive charging has become a primary focus of current research efforts.

In this work, the reproducible trap-controlled ML in $KMgF_3$: Tb^{3+} GCs by UV light pre-irradiation was investigated in details. The inequivalent substitution of Tb^{3+} ions induces intrinsic defects, which can effectively act as trap centers under UV excitation, capturing charge carriers. The thermoluminescence (TL) triggered by frictional heat during mechanical stimulation is the core mechanism behind ML generation. Additionally, elastic composites formed by combining GCs powder with a flexible PDMS medium can achieve self-powered ML through interface triboelectric induction. This indicates that the microscopic physical mechanisms driving ML generation differ across various media, offering valuable guidance for the application of ML materials in diverse fields.

2. Experiments

2.1. Synthesis of $KMgF_3$: Tb^{3+} GCs

A series of glass samples were prepared by melt-quenching method using MgF_2 (97.5 %), K_2CO_3 (99.0 %), SiO_2 (99 %), NaF (98.0 %), Al_2O_3 (99.99 %), and Tb_4O_7 (99.5 %) as raw materials with the following chemical ratios: $13MgF_2$-$21.5K_2CO_3$-$35SiO_2$-13NaF-$17.5Al_2O_3$. The drugs were weighed according to the stoichiometric ratio, ground into powder in an onyx mortar and mixed homogeneously, and then placed in an alumina crucible and melted in a lift-off resistance furnace at 1500 °C for 50 min. The melt was then poured onto a preheated copper plate at 450 °C, and then another copper plate was placed for pressing to form the precursor glass. The samples were cooled to room temperature and heat-treated in a muffle furnace (500 °C) for 2 h, and then annealed in a muffle furnace (620 °C) for 2 h to reduce internal stresses to obtain $KMgF_3$: Tb^{3+} GCs. Finally, the obtained products were polished and cut for further characterization. The drugs were purchased from Aladdin Chemical Reagents Ltd. except K_2CO_3 and NaF, which were purchased from Komeo Chemical Reagents Ltd.

2.2. Preparation of $KMgF_3$: Tb^{3+} GCs/PDMS composite elastomer

2 g of PDMS and 0.2 g of curing agent were mixed in a petri dish with a diameter of 60 mm, and then 1 g of $KMgF_3$: Tb^{3+} GCs powder was weighed into it, and it was stirred and mixed well. Firstly, the petri dish was put into a vacuum oven and degassed for 10 min at room temperature and -80 kPa pressure to remove air bubbles, and then it was put into a Maver oven and heated at 70 °C for 40 min for curing, and finally $KMgF_3$: Tb^{3+} GCs/PDMS composite elastomers were produced.

2.3. Experimental apparatus

The samples were analyzed by X-ray diffraction (XRD) in the range of 10–80° using a Bruk BPUKER D2 PHASER from Germany in the step-and-scan mode. Photoluminescence (PL) and photoluminescence excitation (PLE) spectra of the samples were determined using a Hitachi F-7000 fluorescence spectrometer with a 150-W Xe lamp as the excitation source. The morphology of the samples was then observed by a scanning electron microscope (SEM) TESCAN VEGA 3 SEM (Tescan China, Ltd). The Differential thermal analysis (DTA) curves were recorded using a heating rate of 15 °C/min (STA7300, Japan Corporation, Hitachi High-tech Science). Transmission spectra of the samples were measured in the wavelength range of 200–800 nm using a Hitachi U-4100 spectrophotometer (Hitachi, Tokyo, Japan). After 15 min of UV irradiation, the thermoluminescence (TL) curves of the samples were recorded using LTTL-3DS device (Radiation Tec). The electron paramagnetic resonance (EPR) spectra of the samples were analyzed with the aid of a Bruker X-band A300-6 \ 1 paramagnetic resonance spectrometer at a frequency of 9.2 GHz at RT. The acquisition of the ML signals was accomplished by combining an Ocean Fiber Optic Spectrometer with an MS-T3001 Friction and Wear Tester, with the distance between the friction interface and the electrostatic measurement probe set to 10 cm. During the tensile experiments, the luminescence intensity of the ML was tested and characterized using an Ocean Optics QE Pro fiber optic spectrometer (FLAME-S-XP1-ES) in conjunction with a multimode force luminescence detection system (Qingdao Qingke Longnuo Environmental Technology Co., Ltd. QKLN-ML-2) with a wavelength of 300 nm–1000 nm. The excitation wavelength of the UV light source used in the experiment was 254 nm and the power was 10 W. All optical photographs were taken by a digital camera (Nikon D7100) at RT.

3. Results and discussion

3.1. Phase and structure characterization

Fig. S1(a) shows the XRD patterns of $KMgF_3$: x Tb^{3+} GCs (x = 0.4, 0.6, 0.8, 1.0, and 1.2), and the observed diffraction peaks of the samples match with the (110), (111), and (200) crystallographic planes of the $KMgF_3$ standard card (PDF#18–1033), which suggests that the precipitated microcrystalline phase is $KMgF_3$, and also that the introduction of Tb^{3+} did not form any impurity phase, and the best degree of precipitation was achieved at a Tb^{3+} concentration of 1.0, and the $KMgF_3$: 1.0 Tb^{3+} samples were used for all subsequent tests. Fig. 1(a) shows the XRD pattern of $KMgF_3$: Tb^{3+}. Fig. 1(b) presents the DTA curve of the sample, with the heating rate set at 15 °C/min, aiming to assess the glass transition properties of the sample after annealing treatment. As can be seen from the figure, the glass transition temperature (Tg) is 545 °C. Fig. 1(c) shows the crystal structure of $KMgF_3$, with Mg^{2+} occupying eight vertices of the cube, eight Mg^{2+} surrounding one K^+ to form a central cube, and six F^- surrounding one Mg^{2+} to form a hexahedron. The crystals of $KMgF_3$ are attributed to the Pm3m space group, which belongs to the simple cubic crystal system, and are centrosymmetric. Materials with centrosymmetric structures usually do not exhibit piezoelectric effects because piezoelectric effects require non-centrosymmetric structures to produce coupling between mechanical stresses and electric fields [7,22–24]. The SEM and EDS mapping of the GCs are shown in Fig. 1(d), and it can be seen that the distribution of each element in the sample is homogeneous. The GCs obtained by melt quenching method and heat treatment is a rigid transparent medium. Fig. S1(b) indicates that all the GCs samples have a high transparency with a transmittance above 80 % [25,26]. The PL properties of the samples are shown in Fig. S2, and the optimal excitation and emission spectra of the samples are illustrated in Fig. S2(a). The PL spectrum are composed of four main emission bands, the centers of which are located at 494, 545, 586, 621 nm respectively, which correspond to energy level transitions from $^5D_4$ to ^7F_J (J = 6, 5, 4, 3) [27]. Fig. S2(b) demonstrates the PL spectra of the samples at different Tb^{3+} doping concentrations, and it is observed that the PL intensity increased with doping concentration until 1 % and then decrease due to concentration quenching effect. The CIE coordinates of the $KMgF_3$: Tb^{3+} GCs are given in Fig. S2 (c) with the values of (0.3366,0.4471), which further confirms that the $KMgF_3$: Tb^{3+} GCs exhibits green emission.

3.2. ML performance characterization

It was observed that the ML phenomenon occurred when the fabricated GCs was pre-irradiated with UV light and subsequently rubbed with a sharp object. Fig. S3(a) represents the ML spectra of $KMgF_3$: x Tb^{3+} GCs (x = 0.4, 0.6, 0.8, 1.0, 1.2) applied with friction stimulation, which appears to be similar to the PL spectrum, consisting of characteristic emission peaks of Tb^{3+}, indicating that the ML luminescence

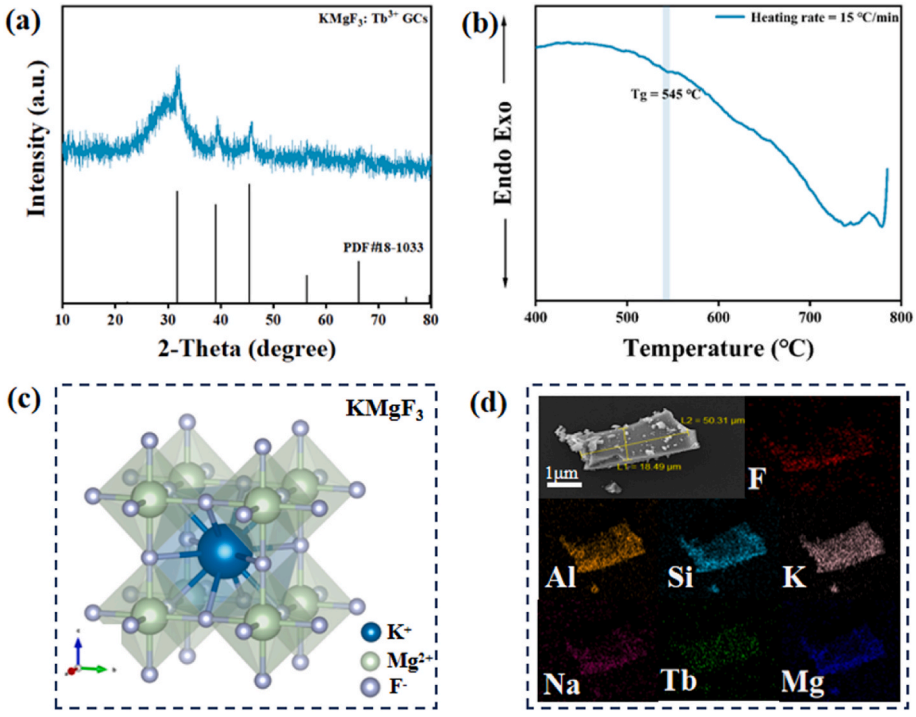

Fig. 1. (a) XRD, (b) DTA, (c) Crystal structure, (d) SEM and EDS Mapping images of $KMgF_3$: 1.0 Tb^{3+} GCs.

center is consistent with that of PL. It also shows that the ML intensity is quenched at a Tb^{3+} doping of 1.0, which is consistent with the PL quenching concentration. Fig. 2(a) shows the ML and PL spectra and luminescence photographs of the samples, which were compared and found to have the same spectral and luminescence colours, and the luminescence is of high brightness and uniformity. Fig. 2(b) shows the variation of ML intensity with applied friction load and the linear fitting results (the corresponding ML spectra are shown in Fig. S3(b)), and the insets are the corresponding ML photos when different loads are applied.

Due to the unique optical waveguide effect of microcrystalline glass, the luminescence of a certain part of the glass will be reflected by a halo around the edge, and with the increasing load, the ML intensity is getting bigger and bigger, and we can observe that the halo is also getting brighter and brighter. As shown in the figure, the ML intensity of $KMgF_3$: Tb^{3+} GCs increases linearly with the applied load, with a linear fitting coefficient of 0.9926. The sensitivity of friction-induced mechanical-optical response is 22.681. Existing studies have shown that the CaF_2: Tb^{3+} crystals are able to produce mechanoluminescence phenomenon

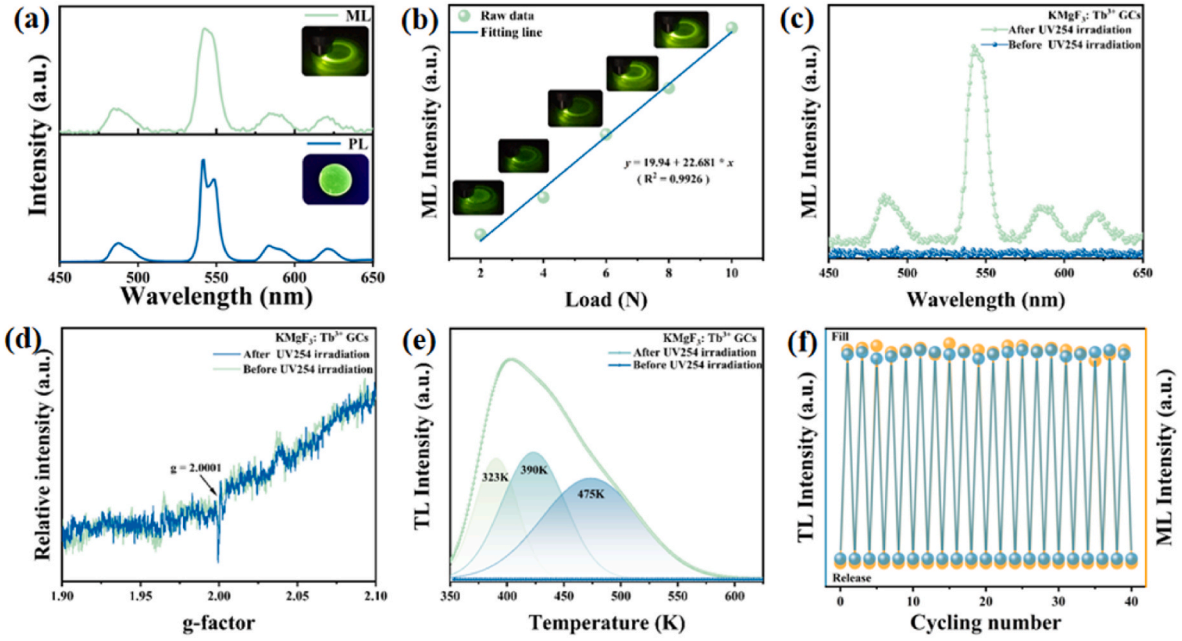

Fig. 2. (a) Spectrograms and photographs of ML and PL.(b) The relationship between ML intensity and applied load of $KMgF_3$: Tb^{3+} GCs (insets shows the corresponding ML photos). (c) ML spectra of $KMgF_3$: Tb^{3+} GCs before and after UV pre-irradiation. (d) EPR spectra of $KMgF_3$: Tb^{3+} GCs before and after UV pre-irradiation. (e) TL curves and fitted results of $KMgF_3$: Tb^{3+} GCs before and after UV pre-irradiation. (f) The cycle stability of ML and TL intensity in 40 cycles.

under the irradiation of X-rays, and the $TbBO_3$ crystals exhibit the same luminescence characteristics under the action of femtosecond laser luminescent properties [18,19], compared with these materials, $KMgF_3$: Tb^{3+} crystals also show excellent performance in the field of stress sensing. Furthermore, a linear relationship was observed between the ML intensity and the friction rate (Figs. S3(c) and S3(d)) at a constant friction load. To investigate the origin of ML in GCs and the effect of UV light pre-charging, the ML spectra before and after UV light pre-irradiation are presented in Fig. 2(c). The GCs without UV light pre-irradiation did not exhibit ML under friction, whereas ML was generated through friction after UV light pre-irradiation. This indicated that UV light irradiation plays a key crucial in the ML production process in GCs.

It is well known that glass materials develop point defects in the glass matrix as a result of photoionization following irradiation with high-energy rays, such as X-ray and femtosecond laser. Since the energy of ultraviolet light is limited and insufficient to generate a significant number of defects in the glass matrix, the traps in $KMgF_3$: Tb^{3+} GCs are likely attributed to intrinsic defects within the $KMgF_3$ crystalline phase. Fig. 2(d) shows the EPR curves of $KMgF_3$: Tb^{3+} GCs sample before and after UV light pre-irradiation. Fig. 2(d) shows the EPR curves of $KMgF_3$: Tb^{3+} GCs before and after UV pre-irradiation. Compared with the pre-irradiation, the EPR signal after UV irradiation is significantly enhanced with a peak at $\approx g = 2.0001$, which is evidence of intrinsic defects in the $KMgF_3$ crystal phase. In materials science, traps refer to certain regions or defects within a material that trap and temporarily immobilise carriers (e.g., electrons or holes). $KMgF_3$: Tb^{3+} GCs are due to the unequal substitution of Tb^{3+} for Mg^{2+}, and the excess positive charge within the host must be compensated for. The only way to achieve equilibrium is for two Tb^{3+} ions to replace three Mg^{2+} ions, which gives two electron defects and one vacancy defect. This is consistent with the conclusions drawn from the analysis of the TL curves. Fig. 2(e) compares the TL curves of $KMgF_3$: Tb^{3+} GCs before and after UV light pre-irradiation. The three distinct TL peaks are observed at 323 K, 390 K, and 475 K, indicating the presence of three types depths trap in $KMgF_3$: Tb^{3+} GCs following UV light irradiation. The size of the energy gap between the electron trap and the conduction band can be obtained by approximate estimation using formula $E\ (eV) = T_m/500(K)$ [28,29], where E represents the thermal activation energy in eV and T_m refers to the peak TL temperature. Accordingly, the depths of the three traps were estimated to be 0.646 eV, 0.78 eV, and 0.95 eV, respectively. Fig. S5(a) presents the TL curves of $KMgF_3$: x%Tb^{3+} GCs ($x = 0.4$, 0.6, 0.8, 1.0, and 1.2), and a decrease in the TL intensity was found at Tb^{3+} doping concentrations above 1.0, which is in agreement with the concentration-quenching phenomenon of PL. To verify the reproducibility of ML under cyclic loading, the samples were irradiated and thermally scavenged 40 consecutive time. The ML and TL intensity data are shown in Fig. 2(f), where it can be observed that the ML intensity remains above 95 % of their initial values. This demonstrates that the ML performance of $KMgF_3$: Tb^{3+} GCs is recoverable. Additionally, and this result indicates a strong correlation between the ML and TL of $KMgF_3$: Tb^{3+} GCs. To further demonstrate the environmental stability of the ML of microcrystalline glass, it was placed in three different environments, namely alcohol, air and underwater, for 0, 2, 4, 6, 8, 10, 1, 12, 14, 16, 18, 20, 22, and 24 h, respectively (Figs. S4(a–c)). It was observed that the $KMgF_3$: Tb^{3+} GCs exhibited good ML stability. This property is attributed to the network-dense structure of the glass network, which provides the internal $KMgF_3$ nanocrystals with a strong protective layer from external environmental factors, ensuring the stable performance of $KMgF_3$ GCs in diverse and harsh environments [30,31]. Fig. S6 shows the temperature-dependent TL photos of the GCs after pre-irradiation with UV lamps for 15 min. It can be seen that the TL of the GCs gradually increases with increasing temperature and slowly decreases after 500 K. The results indicate that room temperature and high temperature thermal stimulation can effectively stimulate the release of carriers in the traps to produce TL after UV light filling. Fig. S5(b) shows the same sample, which was divided into the same nine portions and filled (15 min) at different temperatures (303 K, 353 K, 403 K …) before testing the thermoluminescence curve. The thermoluminescence curve is a plot of the thermoluminescence intensity over a specific temperature range, Fig. S5(b) shows the thermoluminescence intensity of the samples between 300 K and 650 K. Fig. S5(b) shows that the TL intensity decreases as the filling temperature increases, suggesting that the traps are continuously distributed and the carriers are gradually removed as the temperature increases [32]. And it has been previously demonstrated that the ML of GCs correlates well with the TL, proving that the ML intensity correlates with the concentration of charge carriers in the traps, which confirms the speculation on the ML mechanism of $KMgF_3$: Tb^{3+} GCs.

The ML of composite devices in $KMgF_3$: Tb^{3+} GCs powder with different media was also further explored. The ML composite device fabricated process is presents in Fig. 3(a). Firstly, $KMgF_3$: Tb^{3+} GCs was ground into a terminal powder state, composited with a media such as PDMS and then placed in an oven and dried until finalized. The ML photos of $KMgF_3$: Tb^{3+} GCs powder composited with PDMS under mechanical stimuli such as tensile, rubbing, tearing and folding are shown in Fig. 3(b). Fig. 3(c) shows the stress-strain curve of $KMgF_3$: Tb^{3+} GCs/PDMS composite elastomers obtained on a tensile testing machine, where the elastic modulus of the composite was determined to be 1.2738 MPa, while its maximum tensile strength reached 1.5931 MPa. It was also found that there was a linear correlation between the ML intensity and the stress variation. Additionally, to explore the effect of different organic media on the ML performance of composite devices, the triboelectric potential of GCs powder with various organic media was studied. Fig. 3(d) shows the surface triboelectric potential of $KMgF_3$: Tb^{3+} GCs powder after rubbing with PDMS, ER, polyurethane (PU), and silica (SG) substrates for 1 min. We found that for ER and PU, the direct transfer of electrons to $KMgF_3$:Tb^{3+} GCs produces positive potentials on the substrates, and the absolute values of the potentials are small. When $KMgF_3$:Tb^{3+} GCs are rubbed with SG or PDMS, the substrate acquires electrons with negative potentials, which is consistent with the model of interfacial friction charge-induced electron bombardment. Under the action of friction electric field, the electrons in the SG and PDMS substrates are accelerated to bombard the $KMgF_3$:Tb^{3+} GCs, which provides a possible pathway for activation/excitation of luminescent centers. No ML was observed during mechanical stimulation (grinding and compression) of the $KMgF_3$:Tb^{3+} GCs/epoxy resin (ER) composite device. When $KMgF_3$:Tb^{3+} GCs powder is combined with a flexible matrix such as PU, SG, PDMS, etc., the composites are deformed considerably at relatively low tensile stress (<5 MPa). From Fig. 3(e), it can be seen that $KMgF_3$:Tb^{3+} GCs/PU has no ML, while $KMgF_3$:Tb^{3+} GCs/SG has a weak ML (its ML spectrum was shown in Fig. S7), and $KMgF_3$:Tb^{3+} GCs/PDMS has a strong ML under the same strain. This indicates that the triboelectric potential of GCs powder with organic media determines its ML performance.

3.3. ML mechanism analysis

Fig. 4(a) and (b) illustrate the schematic diagrams of the $KMgF_3$:Tb^{3+} GCs and $KMgF_3$: Tb^{3+} GC/PDMS ML mechanisms, respectively. For rigid GCs, UV pre-irradiation can effectively fill the intrinsic defects generated by the inequivalent substitution of Mg^{2+} by Tb^{3+} ions in the $KMgF_3$ microcrystalline phase [33]. Under mechanical stimulation, the Joule heat produced by surface friction can induce the release of trapped charge carriers, resulting in TL, which manifests as mechanical stimulation-induced ML. The self-powered ML generated by $KMgF_3$: Tb^{3+} GCs powder encapsulated in flexible, stretchable organic media is attributed to the triboelectric effect at the inorganic-organic interface. In the initial stage, $KMgF_3$: Tb^{3+} GC particles and the polymer chains of SG or PDMS undergo various mechanical stimuli (such as stretching and friction). The friction at the interface generates a triboelectric field, causing electrons to transition from the valence band to the conduction

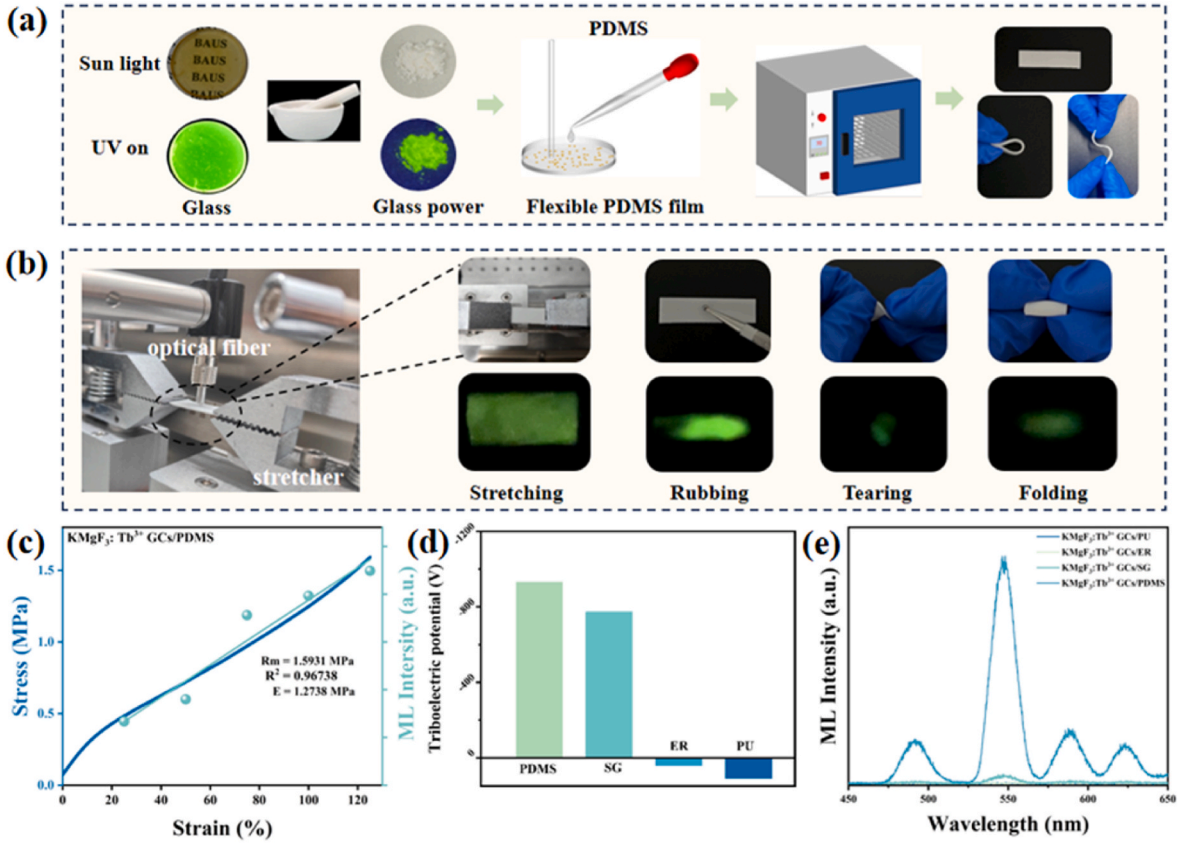

Fig. 3. (a) Schematic diagram of the fabrication for $KMgF_3$: Tb^{3+} GCs/PDMS composite device. (b) ML photos under various mechnacial stimulaition. (c) Stress-strain curve and the relationship between ML intensity and Strain of $KMgF_3$: Tb^{3+} GCs powder/PDMS. (d) The relationship between triboelectric potential and different organic media. (e) ML spectra of $KMgF_3$: Tb^{3+} GCs powder in different media.

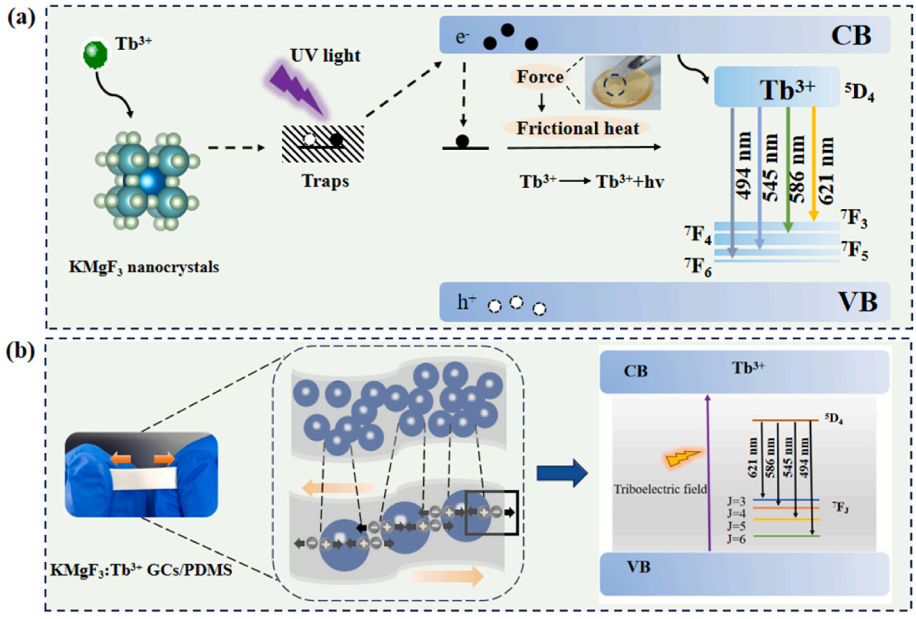

Fig. 4. Schematic diagram of the ML mechanism (a) when friction $KMgF_3$:Tb^{3+} GCs (b) when tension $KMgF_3$:Tb^{3+} GC/PDMS.

band. Subsequently, the electrons in the conduction band transfer to the excited state of Tb^{3+} and recombine with holes in the ground state, triggering ML emission. In the flexible medium, this process enables the conversion of mechanical energy into electrical energy, and finally into optical energy [34–36].

4. Conclusion

Overall, $KMgF_3$: Tb^{3+} GCs microcrystalline glasses were successfully prepared by conventional melt quenching technique in this study. For the first time, high-brightness and reproducible mechanical

luminescence in a rigid medium using a UV lamps as an excitation source has been realized, which is a crucial step in the search for nondestructive microcrystalline glass materials with UV-irradiated ML properties. The use of UV lamps as a means of excitation has the advantages of simplicity, safety, and cost-effectiveness, effectively overcoming the shortcomings of conventional energy replenishment methods. This study realizes rigid/flexible multi-scene ML using the same material by two different ML mechanisms, trap-controlled and friction electric direct excitation, which opens up a new way to realize multi-scene stress detection based on rigid/flexible materials.

CRediT authorship contribution statement

Lili Li: Writing – original draft, Software, Methodology, Investigation, Data curation, Conceptualization. **Yingdan Song:** Supervision, Methodology, Investigation, Conceptualization. **Hongxin Song:** Methodology, Investigation, Data curation. **Kaige Cheng:** Writing – original draft, Software, Methodology, Data curation. **Qiang Xu:** Writing – review & editing, Supervision, Resources, Conceptualization. **Lei Zhao:** Writing – review & editing, Supervision, Software, Resources, Investigation, Conceptualization.

Declaration of competing interest

The authors declare that they have no known competing financial interests or personal relationships that could have appeared to influence the work reported in this paper.

Acknowledgments

This work was supported by the Natural Science Foundation of Shaanxi Province of China (2024JC-YBMS-042), the Youth Innovation Team of Shaanxi Universities, Key Science and Technology Innovation Team of Shaanxi Province (2024RSCXTD66).

Appendix A. Supplementary data

Supplementary data to this article can be found online at https://doi.org/10.1016/j.ceramint.2024.11.044.

References

[1] C. Chen, Z. Lin, H. Huang, X. Pan, T.L. Zhou, H. Luo, L. Jin, D. Peng, J. Xu, Y. Zhuang, R.J. Xie, Revealing the intrinsic decay of mechanoluminescence for achieving ultrafast-response stress sensing, Adv. Funct. Mater. 33 (2023) 2304917.

[2] H. Guo, T. Wang, B. Liu, W. Gao, L. Xiu, Z. Cui, H. Zhang, Q. Ma, S. Wang, Z. Li, L. Guo, G. Yan, S. Yu, X. Yu, X. Xu, J. Qiu, Fabrication and photoluminescence characteristics of novel red-emitting $Ba_2LuNbO_6:Eu^{3+}$ double-perovskite phosphors on near UV WLEDs, J. Rare Earths 40 (2022) 1173–1180.

[3] X. Liu, P. Xiong, L. Li, M. Yang, M. Yang, C. Mao, Monitoring cardiovascular disease severity using near-infrared mechanoluminescent materials as a built-in indicator, Mater. Horiz. 9 (2022) 1658–1669.

[4] Z. Ma, J. Zhou, J. Zhang, S. Zeng, H. Zhou, A.T. Smith, W. Wang, L. Sun, Z. Wang, Mechanics-induced triple-mode anticounterfeiting and moving tactile sensing by simultaneously utilizing instantaneous and persistent mechanoluminescence, Mater. Horiz. 6 (2019) 2003–2008.

[5] D. Tu, C.-N. Xu, Y. Fujio, A. Yoshida, Mechanism of mechanical quenching and mechanoluminescence in phosphorescent CaZnOS:Cu, Light Sci. Appl. 4 (2015) e356.

[6] Y. Zhuang, R.J. Xie, Mechanoluminescence rebrightening the prospects of stress sensing: a review, Adv. Mater. 33 (2021) 2005925.

[7] F. Wang, F. Wang, X. Wang, S. Wang, J. Jiang, Q. Liu, X. Hao, L. Han, J. Wang, C. Pan, H. Liu, Y. Sang, Mechanoluminescence enhancement of ZnS:Cu,Mn with piezotronic effect induced trap-depth reduction originated from PVDF ferroelectric film, Nano Energy 63 (2019) 103861.

[8] Z. Wang, B. Wang, X. Zeng, D. Peng, Y. Wang, Tuning oxygen vacancy in CaZnOS through cation substitution for substantially enhanced multimode luminescence of Mn^{2+} and Tb^{3+}, Adv. Opt. Mater. 11 (2023) 202300623.

[9] P. Zhang, J. Wu, L. Zhao, Z. Guo, H. Tang, Z. Wang, Z. Liu, W. Chen, X. Xu, Environmentally stable and self-recovery flexible composite mechanical sensor based on mechanoluminescence, ACS Sustain. Chem. Eng. 11 (2023) 4073–4081.

[10] Y. Wang, N. Lin, Y. Yue, J. Wang, Y. Li, Z. Wu, S. Xu, G. Bai, Multi-Mode luminescence in smart near-infrared Cr^{3+}/Pr^{3+} codoped $SrGa_{12}O_{19}$ phosphors induced by three distinct excitation mechanisms, ACS Appl. Mater. Interfaces 16 (2024) 33855–33864.

[11] S. Qin, W. Wei, B. Tian, Z. Ma, S. Fang, Y. Wang, J. Zhang, Z. Wang, Self-recoverable, highly repeatable, and thermally stable mechanoluminescence for dual-mode information storage and photonic skin applications, Adv. Funct. Mater. 34 (2024) 2401535.

[12] J. Zhang, W. Wang, S. Wang, Y. Gu, J. Zhou, Contact-separation-induced self-recoverable mechanoluminescence of $CaF_2:Tb^{3+}$/PDMS elastome, Nat. Commun. 15 (2023) 2014.

[13] J. Zhou, Y. Gu, J. Lu, L. Xu, J. Zhang, D. Wang, W. Wang, An ultra-strong non-pre-irradiation and self-recoverable mechanoluminescent elastomer, Chem. Eng. J. 390 (2020) 124473.

[14] Y. Bai, F. Wang, L. Zhang, D. Wang, Y. Liang, S. Yang, Z. Wang, Interfacial triboelectrification-modulated self-recoverable and thermally stable mechanoluminescence in mixed-anion compounds, Nano Energy 96 (2022) 107075.

[15] S. Yu, S. Fang, L. Zhao, Y. Bai, R. Wang, Z. Wang, Self-recoverable and cyclically stable near-infrared mechanoluminescence for dual-mode mechanics visualization and biomechanics detection, Chem. Eng. J. 474 (2023) 145542.

[16] S. Peng, P. Xia, T. Wang, L. Lu, P. Zhang, M. Zhou, F. Zhao, S. Hu, J.T. Kim, J. Qiu, Q. Wang, X. Yu, X. Xu, Mechano-luminescence behavior of lanthanide-doped fluoride nanocrystals for three-dimensional stress imaging, ACS Nano 17 (2023) 9543–9551.

[17] H. Tang, S. Liu, Z. Fang, Z. Yang, Z. Cui, H. Lv, P. Zhang, D. Wang, F. Zhao, J. Qiu, X. Yu, X. Xu, High-resolution X-ray time-lapse imaging from fluoride nanocrystals embedded in glass matrix, Adv. Opt. Mater. 10 (2022) 2102836.

[18] Y. Song, J. Xiao, L. Zhao, Z. Liu, Y. Ling, Y. Yan, Y. Xu, A.N. Yakovlev, T. Hu, T. G. Cherkasova, Q. Xu, C. Wang, X. Xu, Multi-mode mechanoluminescence of fluoride glass ceramics from rigid to flexible media toward multi-scene mechanical sensors, J. Mater. Chem. A 12 (2024) 2796–2806.

[19] J. Xiao, Y. Cai, Y. Song, H. Tang, P. Zhang, Q. Peng, X. Xu, Z. Liu, L. Zhao, High stable mechanoluminescence from $TbBO_3$ GCs for stress safety monitoring, Laser Photon. Rev. 18 (2023) 2301002.

[20] B.V. Zhenya Zhekova-Maradzhieva, Atanas Uzunov, Evgeniya Ivanova, Desislava Petrova, The effect of X-ray radiation on the human body–pros and CONS, RADIATION PROTECTION IN MEDICAL IMAGING AND RADIOTHERAPY SSSP 2 (2016) 161–165.

[21] J. Cao, Y. Ding, R. Sajzew, M. Sun, F. Langenhorst, L. Wondraczek, Mechanoluminescence from highly transparent ZGO:Cr spinel glass ceramics, Opt. Mater. Express 12 (2022) 3238–3247.

[22] L. Li, L. Wondraczek, M. Peng, Z. Ma, B. Zou, Force-induced 1540 nm luminescence: role of piezotronic effect in energy transfer process for mechanoluminescence, Nano Energy 69 (2020) 104413.

[23] M. Li, Z. Wang, X. Zhang, H. Huang, X. Han, X. Wang, P. Li, Piezoelectric-induced mechanoluminescence in centrosymmetric $Lu_3Al_5O_{12}$: properties of self-recoverable and tunable near-infrared luminescence, Chem. Eng. J. 500 (2024) 156715.

[24] X. Wang, D. Peng, B. Huang, C. Pan, Z.L. Wang, Piezophotonic effect based on mechanoluminescent materials for advanced flexible optoelectronic applications, Nano Energy 55 (2019) 389–400.

[25] Y. Li, W. Wang, Y. Pan, H. Chen, Q. Cao, X. Wei, Upconversion luminescence and optical thermometry properties of transparent oxyfluoride glass ceramics embedded with $Ba_4Y_3F_{17}$: Yb^{3+}, Er^{3+} nanocrystals, CrystEngComm 22 (2020) 6302–6309.

[26] Q. Zhang, L. Li, F. Liu, S. Li, X. Wei, W. Wang, H. Chen, Y. Pan, Y. Li, Optical thermometry of Tm^{3+}/Yb^{3+} Co-doped $Ba_3Gd_2F_{12}$ up-conversion glass-ceramic with high sensitivity, J. Solid State Chem. 308 (2022) 122927.

[27] H. Tang, L. Zhao, Z. Liu, Q. Peng, X. Yu, Q. Wang, F. Zhao, M. Deng, Y. Bai, Z. Wang, T. Wang, J. Qiu, X. Xu, A lanthanide-doped glass-ceramic fiber for stress sensing, Cell Rep. Phys. Sci. 3 (2022).

[28] Y. Fu, C. Li, F. Zhang, S. Huang, Z. Wu, Y. Wang, Z. Zhang, Site preference and the optical thermometry strategy by different temperature response from two sites environment of Mn^{2+} in $K_7ZnSc_2B_{15}O_{30}$, Chem. Eng. J. 409 (2021) 128190.

[29] K. Huang, X. Dou, Y. Zhang, X. Gao, J. Lin, J. Qu, Y. Li, P. Huang, G. Han, Enhancing light and X-ray charging in persistent luminescence nanocrystals for orthogonal afterglow anti-counterfeiting, Adv. Funct. Mater. 31 (2021) 2009920.

[30] L. Li, W. Wang, H. Chen, S. Li, Q. Zhang, Y. Pan, Y. Li, Optical thermometry based on upconversion luminescence of $Ba_3Gd_2F_{12}$: Yb^{3+}/Er^{3+} nanocrystals embedded in glass ceramics, J. Non-Cryst. Solids 573 (2021) 121142.

[31] S. Li, W. Wang, X. Wei, L. Li, Q. Zhang, Y. Li, Y. Pan, Luminescent properties of Sr_2LaF_7: Yb^{3+}/Er^{3+} nanocrystals embedded in glass ceramics for optical thermometry, Opt. Mater. 113 (2021).

[32] G. Wang, T. Wang, Y. Yue, L. Hou, W. Huang, X. Zhu, H. Liu, X. Yu, Regulation of Intrinsic Defects of Self-Activated $MgGa_2O_4$ Phosphors for Temperature Dynamic Anti-Counterfeiting, Laser Photonics Rev, 2024 2400793.

[33] N. Li, S. Yu, L. Zhao, P. Zhang, Z. Wang, Z. Wei, W. Chen, X. Xu, Recoverable dual-modal responsive sensing materials based on mechanoluminescence and thermally stimulated luminescence toward noncontact tactile sensors, Inorg. Chem. 62 (2023) 2024–2032.

[34] W. Bu, T. Wang, Y. Wang, W. Huang, L. Guo, Y. Yue, X. Zhu, J. Xiao, X. Yu, Near-Infrared Mechanoluminescence of $Gd_3Ga_5O_{12}$: Cr^{3+}, La^{3+} for Biological Stress Imaging, Laser Photonics Rev., 2024 2400893.

[35] J.-C. Zhang, X. Wang, G. Marriott, C.-N. Xu, Trap-controlled mechanoluminescent materials, Prog. Mater. Sci. 103 (2019) 678–742.

[36] X. Zhang, Z. Li, W. Du, Y. Zhao, W. Wang, L. Pang, L. Chen, A. Yu, J. Zhai, Self-powered triboelectric-mechanoluminescent electronic skin for detecting and differentiating multiple mechanical stimuli, Nano Energy 96 (2022) 107115.